

# Quantum phases of Bose-Einstein condensates with synthetic spin-orbital-angular-momentum coupling

Chunlei Qu, Kuei Sun, and Chuanwei Zhang\*

*Department of Physics, The University of Texas at Dallas, Richardson, Texas 75080-3021, USA*

The experimental realization of emergent spin-orbit coupling through laser-induced Raman transitions in ultracold atoms paves a way for exploring novel superfluid physics and simulating exotic many-body phenomena. A recent proposal with the use of Laguerre-Gaussian lasers enables another fundamental type of coupling between spin and orbital angular momentum (SOAM) in ultracold atoms. We hereby study quantum phases of a realistic Bose-Einstein condensate (BEC) with this synthetic SOAM coupling in a disk-shaped geometry, respecting radial inhomogeneity of the Raman coupling. We find that the experimental system naturally resides in a strongly interacting regime in which the phase diagram significantly deviates from the single-particle picture. The interplay between SOAM coupling and interaction leads to rich structures in spin-resolved position and momentum distributions, including a stripe phase and various types of immiscible states. Our results would provide a guide for an experimental investigation of SOAM-coupled BECs.

PACS numbers: 03.75.Mn, 37.10.Vz, 67.85.-d

## I. INTRODUCTION

The interplay between a single particle's spin and orbital motion, or spin-orbit coupling, plays a crucial role in various nontrivial many-body phenomena, such as topological insulators and superconductors [1, 2] in fermionic systems, as well as exotic spinor condensates and superfluids in bosonic ones. Considerable effort [3–40] has been devoted to the investigation of spin-orbit coupled many-body physics in ultracold atoms due to the system's high tunability, disorder-free environment, and, most importantly, synthetically inducible spin-orbit coupling through the atom-light interaction [41–43]. The recent experimental realization [3–15] of spin and linear momentum (SLM) coupling with the use of counter-propagating Gaussian lasers to induce two-photon Raman transitions [41] enables the direct observation and manipulation of SLM coupled Bose-Einstein condensates (BECs) and degenerate Fermi gases. In spin-orbit coupled BECs, interaction effects are expected to be essential for newly emergent quantum phases [16]. However, compared with the typical kinetic energy scale in the current experimental system, *i.e.* the recoil energy  $E_L = \hbar^2/2M\lambda^2$  with atomic mass  $M$  and the laser's wavelength  $\lambda \sim 1\mu\text{m}$ , the interaction effects are relatively weak such that most behaviors of the SLM coupled BECs show little difference from the single-particle ones [3].

The realization of another fundamental type of spin-orbit coupling, namely the spin-orbital angular momentum (SOAM) coupling, in ultracold atoms has been proposed in our recent work [44], with the use of co-propagating higher-order Laguerre-Gaussian (LG) lasers [44–46] (see Fig. 1). The two LG laser beams with different orbital angular momentum (OAM) stimulate the Raman transitions between two atomic hyper-

fine states,  $|\uparrow\rangle$  and  $|\downarrow\rangle$ , and concurrently impart spin-dependent OAM to the atoms [47–49]. In such a system, the rotational motion defines the kinetic energy scale  $E_0 = \hbar^2/2MR^2$  with  $R \sim 15\mu\text{m}$  of the order of the LG laser's beam waist, which is much smaller than the recoil energy  $E_L$  and thus greatly enhances the many-body effect. Therefore, the SOAM coupled system provides an opportunity to explore the spin-orbit coupled physics in a strongly interacting limit. A SOAM coupled ring BEC has been analyzed to reveal several salient features of the aforementioned physics [44]. However, the effect of the LG laser beams' radial distributions is integrated out and plays no role in the ring system. This inhomogeneous beam intensity will generate radial-dependent potential as well as radial-dependent SOAM coupling in a two-dimensional (2D) system, and it will result in an interesting energetic competition against kinetic energy and interaction.

In this paper, we study the quantum phases of a realistic  $^{87}\text{Rb}$  BEC in a disk-shaped geometry with SOAM coupling. We first discuss the single-particle physics of the 2D system and compute interacting phase diagrams as a function of Raman coupling and detuning with experimental parameters. We then analyze the detailed wavefunctions of each individual phase and show their rich structures attributed to the 2D geometry and interaction.

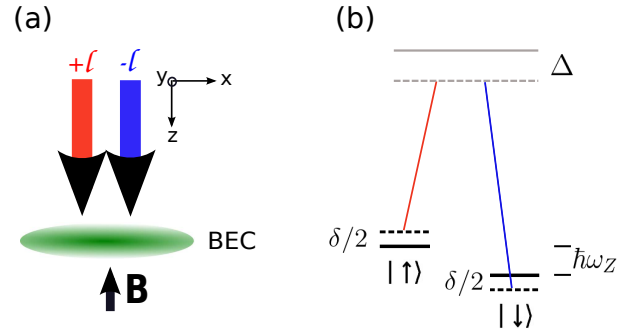


FIG. 1. (Color online) (a) Illustration for generating SOAM coupling and (b) Raman transitions induced by the LG laser beams.

\* Author to whom all correspondence should be addressed: chuanwei.zhang@utdallas.edu

In Sec. II, we build the model Hamiltonian for a SOAM coupled BEC. The single-particle physics is discussed in Sec. III. Section IV presents the main results. We also present the phase diagram of the interacting BEC and discuss the individual phases. In Sec. V, we extend the investigation to the trapping potential and LG beams' OAM-induced quantum phase transitions. Section VI contains the conclusion.

## II. MODEL HAMILTONIAN

We consider a pair of co-propagating LG beams of the semiclassical form ( $j = 1, 2$ )

$$\Omega_j(\mathbf{r}) = \Omega_0 \left( \frac{\sqrt{2}r}{w} \right)^{|l_j|} e^{-\frac{r^2}{w^2}} e^{il_j\phi} e^{ikz} \quad (1)$$

shining on a disk-shaped BEC, where  $(r, \phi, z)$  are the three cylindrical coordinate variables as shown in Fig. 1(a). For simplicity, we assume that the two LG beams have the same amplitudes  $\Omega_0$  and waist  $w$ , but possess opposite OAM  $l_1 = +l$  and  $l_2 = -l$ . We regard the two atomic hyperfine states as two pseudo-spins  $|\uparrow\rangle$  and  $|\downarrow\rangle$ , respectively. Similar to the experiment for SLM coupling [3], an external Zeeman field  $B$  induces a splitting  $\hbar\omega_Z$  between the two states, which also defines the frequency difference of the two LG lasers  $\delta\omega$ . The two pseudo-spins are then coupled through a two-photon Raman transition as illustrated in Fig. 1b. Both LG beams are assumed to be red-detuned from the excited state by  $\Delta < 0$ , while  $\delta = \delta\omega - \hbar\omega_Z$  is the two-photon Raman transition detuning.

The equilibrium and dynamic properties of the BEC with LG beams induced SOAM coupling are governed by the Gross-Pitaevskii (GP) equation  $i\hbar\frac{\partial}{\partial t}\Psi = H_{\text{GP}}\Psi$ , where  $\Psi = (\psi_\uparrow, \psi_\downarrow)^T$  is the spinor wave function of the BEC. The GP Hamiltonian

$$H_{\text{GP}} = \frac{\mathbf{p}^2}{2M} + \tilde{V}_T(\mathbf{r}) + \tilde{V}_{\text{LG}}(\mathbf{r}) + \tilde{V}_I(\mathbf{r}) \quad (2)$$

comprises three potential parts: (1) the external trapping potential  $\tilde{V}_T$ , (2) the LG laser beam potential  $\tilde{V}_{\text{LG}}$ , and (3) the nonlinear mean-field interactions  $\tilde{V}_I$ . Explicitly,

$$\tilde{V}_T = \frac{M}{2} (\omega_x^2 x^2 + \omega_y^2 y^2 + \omega_z^2 z^2), \quad (3)$$

$$\tilde{V}_{\text{LG}} = \tilde{\Omega}_R(r) \begin{pmatrix} 1 & e^{-2il\phi} \\ e^{2il\phi} & 1 \end{pmatrix} - \frac{\delta}{2}\sigma_z, \quad (4)$$

$$\tilde{V}_I = \begin{pmatrix} g_{\uparrow\uparrow}|\psi_\uparrow|^2 + g_{\uparrow\downarrow}|\psi_\downarrow|^2 & 0 \\ 0 & g_{\uparrow\downarrow}|\psi_\uparrow|^2 + g_{\downarrow\downarrow}|\psi_\downarrow|^2 \end{pmatrix}, \quad (5)$$

where  $\omega_{x,y,z}$  are the trapping frequencies, and  $\tilde{\Omega}_R(r) = \frac{|\Omega_1^*(\mathbf{r})\Omega_2(\mathbf{r})|}{4\Delta} = \frac{\Omega_0^2}{4\Delta} \frac{2^l r^{2l}}{w^{2l}} \exp\left(-\frac{2r^2}{w^2}\right)$  is the common factor of the LG laser potential  $\tilde{V}_{\text{LG}}$ , where we have included the Stark shift potential, the Raman coupling, and the detuning terms. The nonlinear interaction coefficients are denoted as  $g_{\sigma\sigma'} = 4\pi\hbar^2 N a_{\sigma\sigma'}^s / M$ , where  $N$  is the

total number of atoms and  $a_{\sigma\sigma'}^s$  is the  $s$ -wave scattering length between the two spins  $\sigma$  and  $\sigma'$ .

Similar to our previous work [44], a unitary transformation  $\psi_{\uparrow/\downarrow} \rightarrow e^{\mp il\phi} \psi_{\uparrow/\downarrow}$  gives

$$H_{\text{GP}} \rightarrow -\frac{\hbar^2}{2Mr^2} (r\partial_r)^2 - \frac{\alpha}{r^2} L_z \sigma_z + \frac{(L_z^2 + \hbar^2 l^2)}{2Mr^2} + \tilde{\Omega}_R(r) \begin{pmatrix} 1 & 1 \\ 1 & 1 \end{pmatrix} - \frac{\delta}{2}\sigma_z + \tilde{V}_T(\mathbf{r}) + \tilde{V}_I(\mathbf{r}). \quad (6)$$

The second term in the above rotated Hamiltonian is an effective SOAM coupling of the form  $\frac{\alpha}{r^2} L_z \sigma_z$ , where  $\alpha = \frac{\hbar l}{M}$  describes the coupling strength and  $L_z = -i\hbar\partial_\phi$  is the  $z$ -component OAM operator. One can see explicitly the radial dependence  $\propto r^{-2}$  of SOAM coupling, which constitutes a key ingredient in our 2D model.

The extrema of the LG beam potential along the radial direction occurs at  $R = \sqrt{l/2w}$ . Below we use  $R$ ,  $k_r = 1/R$ , and  $E_r = \hbar^2 k_r^2 / 2M$  as the length, momentum, and energy units, respectively. The LG beam potential can thus be written in a dimensionless form

$$V_{\text{LG}} = \Omega e^{-lr^2} r^{2l} \begin{pmatrix} 1 & e^{-2il\phi} \\ e^{2il\phi} & 1 \end{pmatrix}, \quad (7)$$

where  $\Omega = \frac{\Omega_0^2 l}{4\Delta E_r}$  is the only dimensionless variable for tuning  $V_{\text{LG}}$  at fixed  $l$ . In addition, we consider a harmonic trap  $\omega_x = \omega_y \ll \omega_z$  that strongly confines the BEC along the  $z$  direction, so the system is well described by a 2D GP Hamiltonian. The 2D trapping potential can be written in a dimensionless form as  $V_{\text{trap}}(r) = \frac{1}{2} K r^2$ , where  $K = M^2 \omega_x^2 l^2 w^4 / 2\hbar^2$  is the dimensionless trapping strength. In the next section, we will study the single-particle physics with the dimensionless expression and present the ground state diagram as a function of LG beam as well as the external trapping potentials.

## III. NON-INTERACTING CASE

Without interactions,  $\tilde{V}_I = 0$ , and the GP Hamiltonian becomes a Schrödinger one. Due to cylindrical symmetry, the eigenstates can be described by an angular quantum number  $m$  as well as a radial one  $n$  and can be written in a form of  $(\chi_{\uparrow,n}(r)e^{im_\uparrow\phi}, \chi_{\downarrow,n}(r)e^{im_\downarrow\phi})^T$  with  $m_{\uparrow/\downarrow} = m \mp l$  [46]. The angular number  $m$  is an integer because OAM quantization of each spin component requires  $m_{\uparrow/\downarrow}$  to both be integers. The OAM difference  $m_\uparrow - m_\downarrow = -2l$  comes from the effect of the SOAM coupling. The radial number  $n$  is a non-negative integer due to the radial confinement and describes the number of radial nodes of the wave function. For a given  $m$ , the radial part of the wavefunctions  $\Psi_n(r) = (\chi_{\uparrow,n} \ \chi_{\downarrow,n})^T$  and corresponding eigenenergies  $E_{n,m}$  can be obtained by solving a radial Schrödinger equation,

$$E\Psi = \left[ -\frac{1}{r}\partial_r(r\partial_r) + \frac{K}{2}r^2 + \frac{1}{r^2} \begin{pmatrix} m_\uparrow^2 & 0 \\ 0 & m_\downarrow^2 \end{pmatrix} + \Omega e^{-lr^2} r^{2l} \begin{pmatrix} 1 & 1 \\ 1 & 1 \end{pmatrix} \right] \Psi, \quad (8)$$

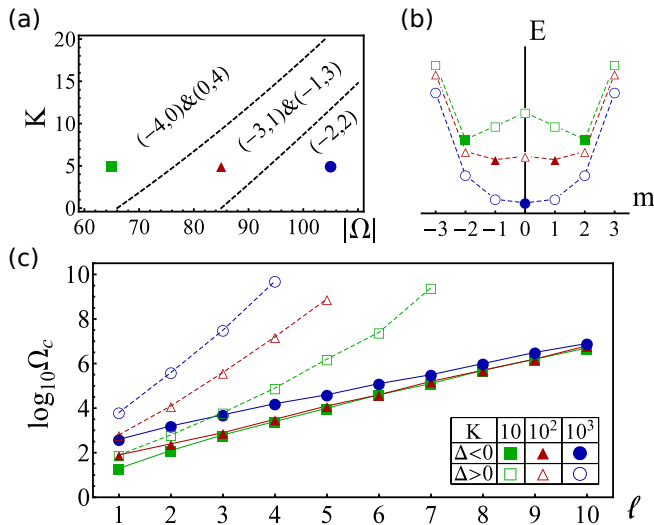


FIG. 2. (Color online) (a) Non-interacting state diagram in  $K$ - $|\Omega|$  plane. Different states denoted with OAM quantum numbers  $(m_\uparrow, m_\downarrow)$  separate by dashed lines. (b) Energy spectrum of the lowest band  $n = 0$  as a function of quasi-OAM  $m$  at select points (square, triangle, and circle) in (a). The filled symbols denote the ground states. (c) Critical value of Raman coupling from double-minima to single-minimum transition for blue ( $\Delta > 0$ ) and red ( $< 0$ ) detuned lasers and for different trapping strengths  $K$ .

where we assume  $\delta = 0$ . We find that  $E_{n,m}$  always increases with  $n$ , so it is convenient to interpret the energy spectrum by regarding  $n$  as a band index. The ground state thus lies in the lowest band of  $n = 0$ . If we treat  $m$  as a quasi-OAM number, the lowest band structure  $E_{0,m}$  can exhibit either double minima at  $m = \pm m_0$  with  $0 < m_0 \leq l$  or a single minimum at  $m = 0$ , determined by  $\Omega$  and  $K$ .

In Fig. 2(a), we plot the ground state diagram in  $|\Omega|$ - $K$  plane for the case of  $l = 2$  and  $\Delta < 0$ . Each region is labeled by the ground-state OAM numbers  $(m_\uparrow, m_\downarrow)$  for each spin species. At a fixed  $K$ , the system undergoes transitions from the degenerate ground states  $m = \pm 2$  to  $m = \pm 1$ , and to the single one  $m = 0$  as  $|\Omega|$  increases. We also find that the spin polarization has the same sign as  $m$  and becomes zero if  $m = 0$ . Both characteristics show similar physics to that in SLM coupled BEC or SOAM coupled ring BEC. Figure 2(b) shows the lowest band for selected points at  $K = 5$  in Fig. 2(a). One can see how the band structure evolves between different ground states. At a fixed  $\Omega$ , we find that  $K$  competes with  $\Omega$  and moves the system from the single-minimum region toward the double-minimum ones. This trend can be understood as a result of energetic competition. The external trap tends to concentrate the BEC around the central region to reduce the potential energy, but rotational energy from the centrifugal barrier  $r^{-2}m_{\uparrow/\downarrow}$  in Eq. (8) strongly increases unless the OAM number vanishes. As a result, the system favors the majority spin component having a low or zero angular momentum and localizing around the trap center, even with a certain energetic penalty from the minority component and from SOAM coupling. In Fig. 2(c), we plot the critical strength  $\Omega_c$  of SOAM

coupling for the transition between degenerate and non-degenerate ground states as a function of  $l$  at various  $K$  and different signs of  $\Delta$ . We see that  $\Omega_c$  increases with increasing  $l$ , increasing  $K$ , or blue-detuned  $\Delta > 0$ , consistent with the same physical picture of BEC's avoiding higher rotational energy. Note that the blue-detuned  $\Delta$  centers the BEC more because the Stark shift creates a ring-shaped barrier around the high intensity region of the LG beams.

Before studying the interaction effect, we comment on an interesting case, where the difference between two LG beams' azimuthal indices  $l_1 - l_2$  is an odd number. In this case,  $m_{\uparrow/\downarrow} = m \mp (l_1 - l_2)/2$  indicates that  $m$  should be a half-integer to satisfy OAM quantization. As  $\Omega$  increases from zero, the magnitude of  $m$  suppresses from  $|(l_1 - l_2)/2|$  until  $m = \pm 1/2$ . Therefore, the lowest band always has a double-minima structure and the system always has two degenerate ground states with opposite spin polarization.

## IV. INTERACTING CASE

### A. Phase diagram

In this section, we focus on a realistic  $^{87}\text{Rb}$  system, compute the full phase diagram, and characterize each individual phase as well as various phase transitions. We consider two atomic internal states  $|\uparrow\rangle = |F = 1, m_F = 0\rangle$  and  $|\downarrow\rangle = |F = 1, m_F = -1\rangle$  of  $^{87}\text{Rb}$  atoms that are coupled through the Raman transitions induced by the two LG laser beams with  $l = 2$ . The radial intensity waist of the LG beam is  $w = 12\sqrt{2}\mu\text{m}$ , which gives  $R \approx 17\mu\text{m}$  and  $E_r = 2\pi\hbar \times 0.2 \text{ Hz}$ . The  $z$ -direction trapping frequency  $\omega_z = 2\pi \times 600\text{Hz}$  is set large enough such that the system has an effective 2D geometry [50], while the transverse trapping frequency  $\omega_x = \omega_y = 1.5 \sim 6.0 \text{ Hz}$  is set isotropic. The  $s$ -wave scattering lengths are  $a_{\uparrow\uparrow} = 100.86a_B$  and  $a_{\downarrow\downarrow} = 100.4a_B$  for  $^{87}\text{Rb}$ , where  $a_B$  is the Bohr radius. In a case of particle number  $N = 10^4$ , the reduced 2D nonlinear interaction energy  $E_I \gg E_r$  is much larger than the single-particle rotational energy. Such strong nonlinear interaction will drastically modify the single-particle physics, as we will see. Note that with this setup, the three nonlinear coefficients satisfy  $g_{\uparrow\uparrow}g_{\downarrow\downarrow} > g_{\uparrow\downarrow}^2$ , which indicates that a rotating spinor BEC without the Raman dressing should be miscible [51]. However, we shall see that the wavefunctions of opposite spins can be spatially separated or immiscible in the presence of SOAM coupling.

We obtain the ground state by solving the GP equation using the imaginary-time evolution. Figure 3 shows the phase diagram in the Raman coupling and detuning  $\Omega$ - $\delta$  plane, where the colors denote the spin polarization. For comparison, we present the non-interacting and interacting phase diagrams in Figs. 3(a) and 3(b), respectively. We see that there are four different phases in the interacting case according to the spin polarization  $\langle\sigma_z\rangle$  and OAM of the two spins  $(m_\uparrow, m_\downarrow)$ : (i) A stripe phase with a density modulation in the angular direc-

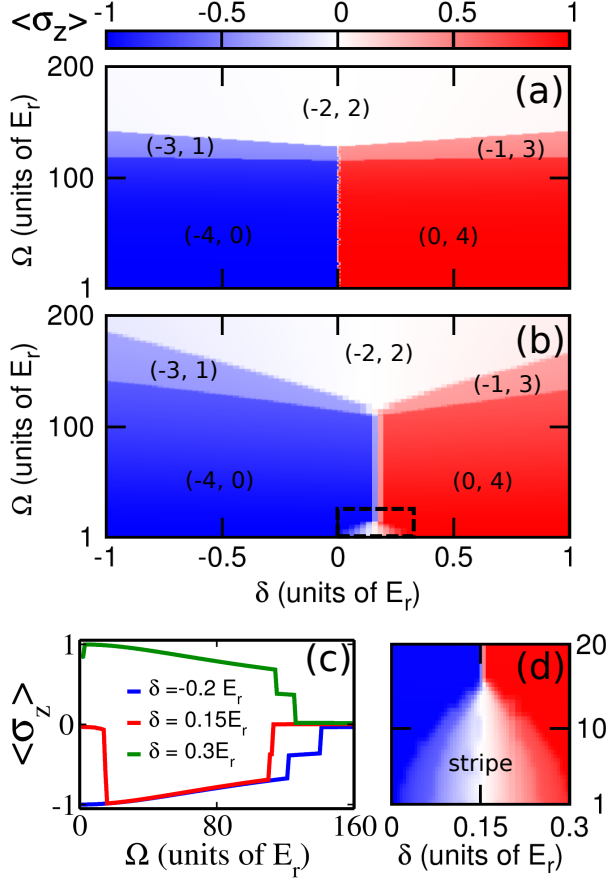


FIG. 3. (Color online) Phase diagram of the SOAM coupled BEC in  $\Omega$ - $\delta$  plane for (a) non-interacting system and (b) realistic BEC. The colors defined in the bar graph represent spin polarization  $\langle \sigma_z \rangle$ . A stripe phase with small polarization occurs at the bottom of (b). The other phases are labeled by their OAM numbers of the two spin components ( $m_\uparrow, m_\downarrow$ ). (c) Spin polarization as a function of Raman coupling  $\Omega$  for detuning  $\delta = -0.2, 0.15$ , and  $0.3 E_r$ . (d) Zoom-in of the dashed region in (b) showing the stripe phase. Other parameters are  $\omega_x = \omega_y = 1.5 \text{ Hz}$ ,  $N = 1 \times 10^4$ , and  $l = 2$ .

tion that is the superposition of  $(-4, 0)$  and  $(0, 4)$  states; (ii) a spin-polarized phase, either  $(-4, 0)$  or  $(0, 4)$ ; (iii) a spin-polarized phase, either  $(-3, +1)$  or  $(-1, +3)$ ; and (iv) a spin-balanced phase  $(-2, 2)$ . We comment that the energy difference between these phases can be small (compared with typical trapping potential energy, SOAM coupling energy, and kinetic energy), and BEC may end up with a metastable state in our numerical simulation. To obtain the ground-state phase boundaries accurately, we start from several initial states to do the imaginary-time evolution and choose a final state with the lowest energy as the true ground state of the interacting BEC. The convergence tolerance of the GP calculation is chosen as  $10^{-4} E_r$  such that the energy difference between the ground state and any metastable state is clearly discernible. We also emphasize that the ground state of the system is robust against small perturbations due to both the energy gap from other metastable states and OAM quantization. Compared with the single-particle phase

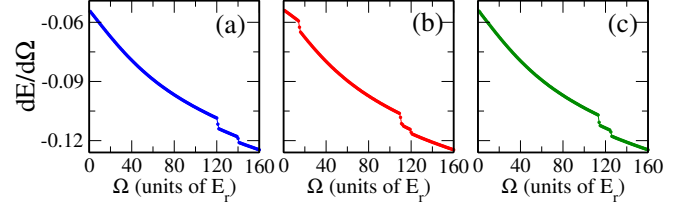


FIG. 4. (Color online) The derivative of ground state energy  $dE/d\Omega$  as a function of Raman coupling strength  $\Omega$  for (a)  $\delta = -0.2 E_r$ , (b)  $\delta = 0.15 E_r$ , (c)  $\delta = 0.3 E_r$ . Compared with Fig. 3(c), we see the phase transition is first order where the energy derivative is discontinuous whenever the spin polarization jumps.

diagram of Fig. 3(a), we see that the interaction shifts the phase boundaries and induces a stripe phase [Fig. 3(b)] that is described by a state with density modulations. Different from the SLM coupling case, the density modulation here is along the angular direction. In Fig. 3(c), we plot the spin polarization as a function of Raman coupling for various detunings. Figure 3(d) is the enlarged stripe phase where the spin polarization is zero or small. The reason why the stripe phase is not symmetric around  $\delta = 0$  is because of the scattering length difference of the two spins, which contributes an effective detuning, similar to the SOAM coupled ring BEC [44]. Here we see the premium detuning value is about  $\delta = +0.15 E_r$ . In Fig. 4, we plot the energy derivative  $dE/d\Omega$  as a function of Raman coupling. Compared with Fig. 3(c), we see that the energy derivative is discontinuous whenever the spin polarization jumps or OAM changes, indicating that the phase transitions are first order.

We shall see in the next section that each phase can exhibit richer structures in the spin-density distribution, including a phase separation in a large parameter region: the two spins can be immiscible due to SOAM coupling and interaction. In this case, the wave function of the two spins is not exactly of the form  $\chi_\sigma(r) e^{im_\sigma \phi}$  as in the non-interacting case. However, one can still find a set of integer winding numbers ( $m_\uparrow, m_\downarrow$ ) by integrating the phase of each spin's wavefunction over a path enclosing the system. Such winding numbers satisfy  $m_\uparrow - m_\downarrow = -2l$  and lock with the spin polarization. Therefore, similar to the OAM numbers in the non-interacting case, they are good quantum numbers for distinguishing different phases in the presence of interaction, although the system may show different types of phase separation at a given  $(m_\uparrow, m_\downarrow)$ .

## B. Individual phases

In this section, we discuss the individual phases along the  $\delta = +0.15 E_r$  line in the phase diagram of Fig. 3(b) in more details.

For very weak Raman coupling and small detuning, we see that the system prefers a stripe phase as shown in Fig. 5(a). The two spins have density modulations in the angular direction, which arise from the fact that there are two degenerate dressed states with similar weight at quasi-OAM  $m = -2$  and  $m = +2$  [green squares in



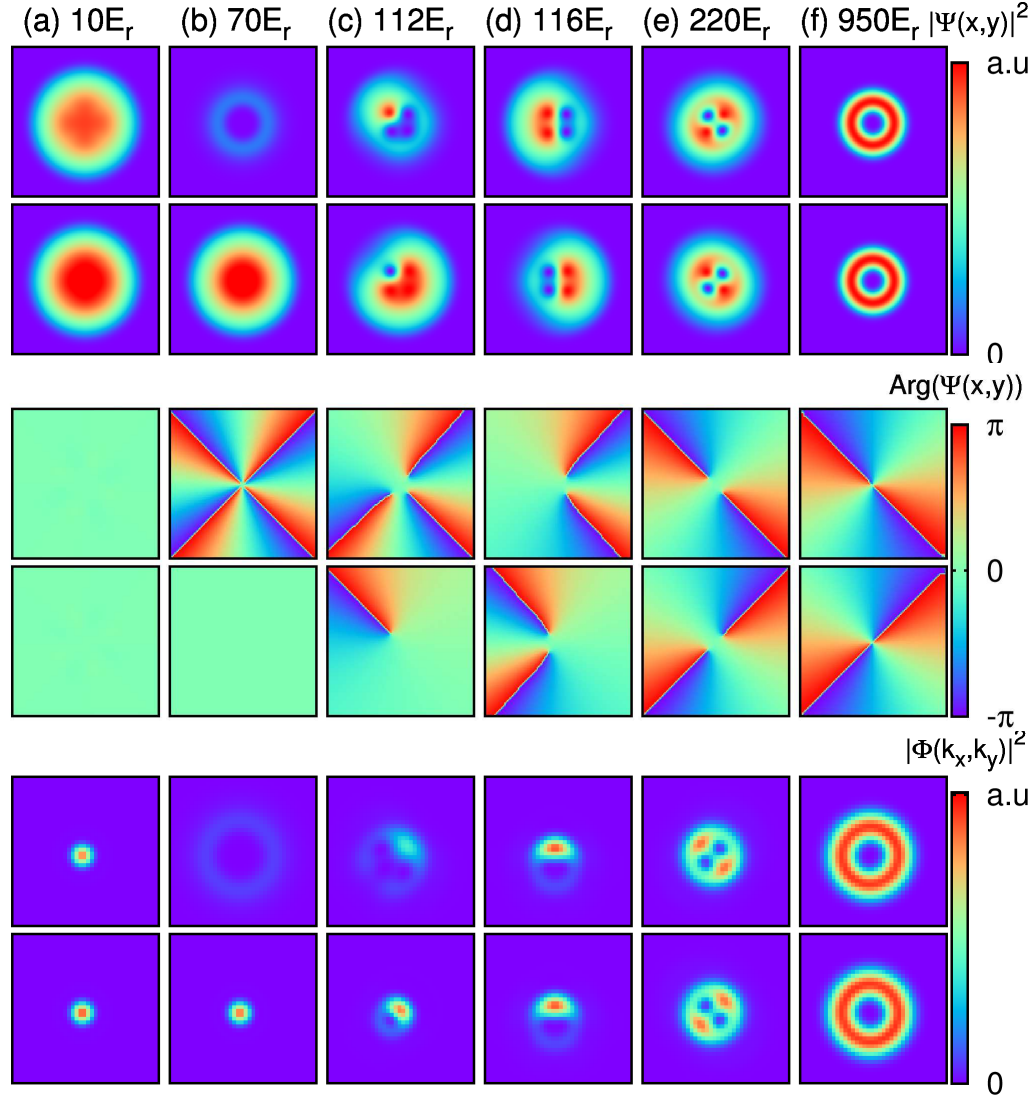


FIG. 5. (Color online) Spin-resolved density distributions of up (upper panel) and down (lower) spins at Raman coupling strengths (a)  $10E_r$ , (b)  $70E_r$ , (c)  $112E_r$ , (d)  $116E_r$ , (e)  $220E_r$ , and (f)  $950E_r$ . The top two rows show the real space density distributions, the middle two do the wavefunction phases, and the bottom two do the momentum distributions. The Raman detuning is  $\delta = +0.15E_r$ . The displayed range of the axis is  $[-57\mu m, +57\mu m]$  in real space and  $[-6k_r, 6k_r]$  in momentum space. All other parameters are the same as Fig. 3.

Fig. 2(b)] that interfere with each other in the real space. Because of the superposition of two dressed states, the phase  $[\text{Arg}(\Psi)]$  of the two spins in the stripe phase is almost uniform and their momentum space distributions ( $|\Phi|^2$ ) are centered at  $\mathbf{k} = 0$ .

With the increase of the Raman coupling, there is a competition between the stripe phase and the occupation of a single dressed-state phase. In the SLM coupling case, the stripe phase occupies a small parameter region and the transition to the single dressed state occurs around  $\Omega \sim 0.2E_r$ . However, here we see that the critical value for this transition is about  $\Omega \sim 15E_r$  in the SOAM coupling system. When the particle number or the angular momentum  $l$  is increased, this parameter region may be even larger. Note that the stripe phase has never been observed experimentally yet in the SLM coupling system because of its small parameter region and the stringent requirement to resolve the density modulations separa-

tions (which are at the order of  $\lambda \sim 1\mu m$ ). It might be easier to resolve the density modulation separations (which are at the order of  $R \sim 10\mu m$ ) in the SOAM coupled BEC.

In Fig. 5(b), we show a single dressed-state phase, where one of the spin states does not carry any OAM and the other spin carries the largest OAM, *i.e.*  $m_\uparrow = 0$  and  $m_\downarrow = 4$ . Because of their different OAM, the density of up spin is of a rotationally symmetric Gaussian shape, while that of down spin is of a ring shape with a hollowed center. Similar features are obtained in the momentum space density distributions.

When the Raman coupling is strong enough, the two spins may both carry OAM as shown in Figs. 5(c)–5(e), where we have  $(m_\uparrow, m_\downarrow) = (-1, +3)$  or  $(-2, +2)$ . This transition can be understood from the single-particle physics picture, where the lowest-energy band evolves from a double minima region to a single minimum re-

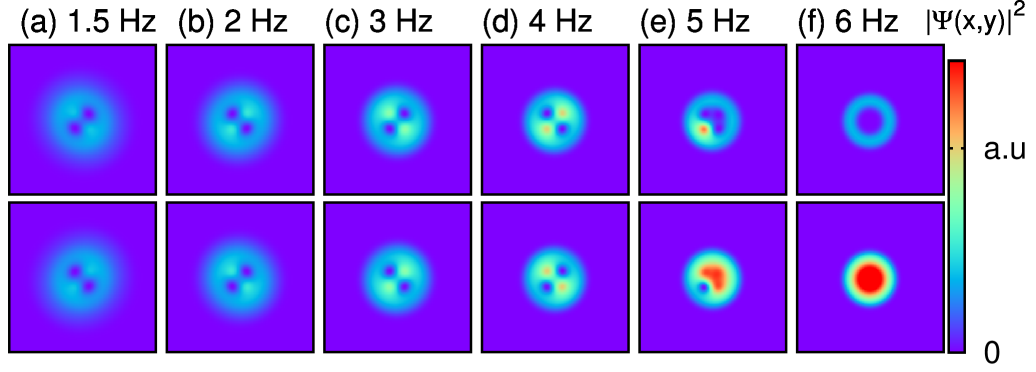


FIG. 6. (Color online) Density distribution of spin up (upper panel) and spin down (lower) for different trapping frequencies (a) 1.5Hz, (b) 2Hz, (c) 3Hz, (d) 4Hz, (e) 5Hz, and (f) 6Hz at  $\delta = 0E_r$  and  $\Omega = 250E_r$ . The displayed range of the axis is  $[-57\mu m, +57\mu m]$  in real space. All other parameters are the same as in Fig. 3.

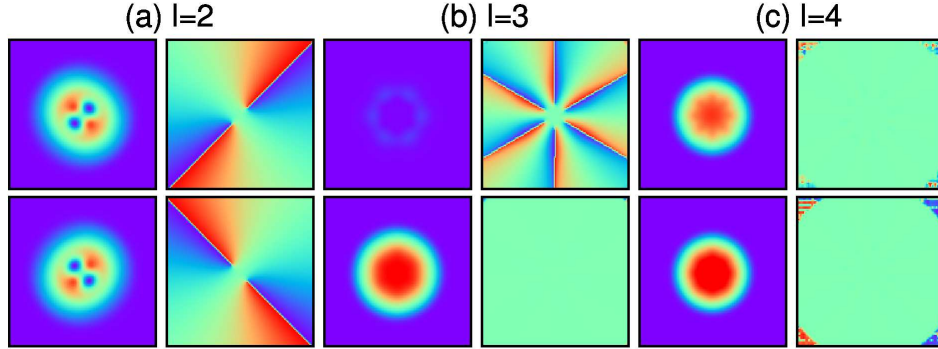


FIG. 7. (Color online) Real-space density distribution and phase of spin up (upper panel) and spin down (lower panel) for LG lasers of different OAM (a)  $l = 2$ , (b)  $l = 3$ , and (c)  $l = 4$  at  $\delta = 0$  and  $\Omega = 250E_r$ . For each figure, the left side is the real-space density distribution and the right side is the phase of the wave function. The displayed range of the axis is  $[-57\mu m, +57\mu m]$  in real space. All other parameters are the same as in Fig. 3.

gion. However, an interesting result shows that the two spin components appear to be immiscible or spatially separated, *i.e.*, wherever one spin dominates, the other spin is strongly suppressed. The phase separation occurs in a large parameter region of  $\Omega = 110 \sim 800E_r$  in Fig. 3(b) when both spin components carry OAM. The emergence of phase separation can be understood from the perspective of lowering nonlinear interaction energy  $\sim \int \int (\rho_{\uparrow} + \rho_{\downarrow})^2 dx dy$ . When the two spins both carry angular momentum and are not separated, the total density of the system must have a hollowed density at the trap center. The total nonlinear interaction energy of this system is usually larger than the separated phase where the total density distribution does not have a hollowed center but instead is in a Gaussian shape [51, 52].

Among these immiscible states, the two spins carrying opposite OAM  $+2$  and  $-2$  display very interesting density distributions, as shown in Figs. 5(d) and 5(e): the two holes and two peaks of the two spin components could appear in a dipole (d) or quadrupole (e) form. We also verify that there are more complicated and rich separated phases for larger  $l$ . The momentum distributions of each of the two states are quite different and may be distinguished in the time-of-flight experiments.

In Fig. 5(f), we plot the density distributions of the two spins for a very large Raman coupling  $\Omega = 950E_r$ . When the LG beam intensity is too strong,  $\Omega > 800E_r$ ,

both components are trapped around the potential minimum of  $V_{LG}$  and forced to mix with each other. Note that the Raman coupling and the Stark shift form an effective ring-shaped optical trap, which is even deeper than the harmonic trap center for such a larger Raman coupling strength. In this case, the two components exhibit a miscible ring distribution and their momentum distributions are also of a ring-shape, which returns to the ring limit [44].

## V. HARMONIC TRAP AND OAM INDUCED PHASE TRANSITION

In this section, we study the effects of the harmonic trapping potential and larger OAM number of the LG beams. From the single-particle results in Fig. 2(c), we see that the trapping strength may drive a quantum phase transition between the states with different OAM. In Fig. 6, we plot the real-space density distributions of the two spins with increasing trapping potential from 1.5Hz to 6Hz. The two spins are pushed inward when the trapping potential is increased and the OAM of the two spins changes from  $(-2, 2)$  to  $(-3, 1)$  and then  $(-4, 0)$ , which is consistent with the energetic competition described in Sec. III. In previous SLM coupled systems, the trapping strength was relatively weak and thus there were no observable effects with the change of trapping

frequencies. Our results demonstrate that the SOAM coupled BEC has a significant response to the trapping potential.

In Fig. 7, we plot the density distributions and phases of the two spins for (a)  $l = 2$ , (b)  $l = 3$ , and (c)  $l = 4$ . We see that the two spins are in a  $(-2, 2)$  separated phase for  $l = 2$ , then in the  $(-6, 0)$  spin-polarized miscible phases for  $l = 3$ , and eventually a stripe phase from the superposition of  $(-4, 0)$  and  $(0, +4)$  dressed states for  $l = 4$ . This can be understood from the  $l$  dependence of the critical Raman coupling strength, similar to the single-particle results in Fig. 2(c).

## VI. CONCLUSION

In conclusion, we studied the quantum phases of a SOAM coupled BEC with realistic experimental parameters in a 2D geometry. The phase diagram shows distinct physics from a SLM coupled BEC due to the naturally strong interaction and OAM quantization, and even from a SOAM coupled ring BEC due to the radial inhomogeneity. The interaction-induced stripe phase and different

immiscible states have been characterized by the spin-resolved position and momentum distributions. Various quantum phase transitions induced by the Raman coupling, detuning, trapping potential, or LG beams' OAM have been reported too. Although the results are presented for  $^{87}\text{Rb}$  atoms, our model and treatment can be easily applied on others such as  $^{23}\text{Na}$ . For a typical Raman coupling strength of 1 kHz and an experimental time scale of 1 s, the heating effects in both  $^{87}\text{Rb}$  and  $^{23}\text{Na}$  systems should be weak [28, 44].

Since the dynamics of ultracold atoms under the application of LG beams have been experimentally investigated by several groups [53–58], and ongoing experimental effort is along this direction for the realization of SOAM coupling [59], the achievement of a BEC ground state with SOAM coupling would be expectable in the near future. Our results hence provide timely predictions for experimental observation.

**Acknowledgements:** We are grateful to L. Jiang and Y. Xu for interesting discussions. This work is supported by ARO (W911NF-12-1-0334) and AFOSR (FA9550-13-1-0045).

- 
- [1] M. Z. Hasan and C. L. Kane, *Colloquium: Topological insulators*, *Rev. Mod. Phys.* **82**, 3045 (2010).
  - [2] X.-L. Qi and S.-C. Zhang, *Topological insulators and superconductors*, *Rev. Mod. Phys.* **83**, 1057 (2011).
  - [3] Y.-J. Lin, K. Jiménez-García and I. B. Spielman, *Spin-orbit-coupled Bose-Einstein condensates*, *Nature*, **471**, 83-86 (2011).
  - [4] Z. Fu, P. Wang, S. Chai, L. Huang, and J. Zhang, *Bose-Einstein condensate in a light-induced vector gauge potential using 1064-nm optical-dipole-trap lasers*, *Phys. Rev. A* **84**, 043609 (2011).
  - [5] J. -Y. Zhang, S.-C. Ji, Z. Chen, L. Zhang, Z. -D. Du, B. Yan, G.-S. Pan, B. Zhao, Y. -J. Deng, H. Zhai, S. Chen, and J. -W. Pan, *Collective Dipole Oscillations of a Spin-Orbit Coupled Bose-Einstein Condensate*, *Phys. Rev. Lett.* **109**, 115301 (2012).
  - [6] C. Qu, C. Hamner, M. Gong, C. Zhang, and P. Engels, *Observation of Zitterbewegung in a spin-orbit-coupled Bose-Einstein condensate*, *Phys. Rev. A* **88**, 021604(R) (2013).
  - [7] S.-C. Ji, J.-Y. Zhang, L. Zhang, Z.-D. Du, W. Zheng, Y.-J. Deng, H. Zhai, S. Chen, and J.-W. Pan, *Experimental determination of the finite-temperature phase diagram of a spin-orbit coupled Bose gas*, *Nat. Phys.* **10**, 314 (2014).
  - [8] C. Hamner, C. Qu, Y. Zhang, J. Chang, M. Gong, C. Zhang, and P. Engels, *Dicke-type phase transition in a spin-orbit-coupled Bose Einstein condensate*, *Nat. Commun.* **5**, 4023 (2014).
  - [9] A. J. Olson, S.-J. Wang, R. J. Niffenegger, C.-H. Li, C. H. Greene, Y. P. Chen, *Tunable Landau-Zener transitions in a spin-orbit-coupled Bose-Einstein condensate*, *Phys. Rev. A* **90**, 013616 (2014).
  - [10] K. Jimenez-García, L. J. LeBlanc, R. A. Williams, M. C. Beeler, C. Qu, M. Gong, C. Zhang, and I. B. Spielman, *Tunable Spin-Orbit Coupling via Strong Driving in Ultracold-Atom Systems*, *Phys. Rev. Lett.* **114**, 125301 (2015).
  - [11] D. L. Campbell, R. M. Price, A. Putra, A. Valdés-Curiel, D. Trypogeorgos, and I. B. Spielman, *Itinerant magnetism in spin-orbit coupled Bose gases*, *arXiv:1501.05984*.
  - [12] P. Wang, Z.-Q. Yu, Z. Fu, J. Miao, L. Huang, S. Chai, H. Zhai, and J. Zhang, *Spin-Orbit Coupled Degenerate Fermi Gases*, *Phys. Rev. Lett.* **109**, 095301 (2012).
  - [13] L. W. Cheuk, A. T. Sommer, Z. Hadzibabic, T. Yefsah, W. S. Bakr, and M. W. Zwierlein, *Spin-Injection Spectroscopy of a Spin-Orbit Coupled Fermi Gas*, *Phys. Rev. Lett.* **109**, 095302 (2012).
  - [14] R. A. Williams, M. C. Beeler, L. J. LeBlanc, K. Jiménez-García, and I. B. Spielman, *Raman-Induced Interactions in a Single-Component Fermi Gas Near an s-Wave Feshbach Resonance*, *Phys. Rev. Lett.* **111**, 095301 (2013).
  - [15] Z. Fu, L. Huang, Z. Meng, P. Wang, L. Zhang, S. Zhang, H. Zhai, P. Zhang, and J. Zhang, *Production of Feshbach molecules induced by spin-orbit coupling in Fermi gases*, *Nat. Phys.* **10**, 110 (2014).
  - [16] V. Galitski and I. B. Spielman, *Spin-orbit coupling in quantum gases*, *Nature* **495**, 49 (2013).
  - [17] X. Zhou, Y. Li, Z. Cai, C. Wu, *Unconventional states of bosons with the synthetic spin-orbit coupling*, *J. Phys. B: At. Mol. Opt. Phys.* **46**, 134001 (2013).
  - [18] H. Zhai, *Degenerate quantum gases with spin-orbit coupling: a review*, *Rep. Prog. Phys.* **78**, 026001 (2015).
  - [19] C. Wang, C. Gao, C.-M. Jian, and H. Zhai, *Spin-Orbit Coupled Spinor Bose-Einstein Condensates*, *Phys. Rev. Lett.* **105**, 160403 (2010).
  - [20] C. Wu, I. Mondragon-Shem, and X.-F. Zhou, *Unconventional Bose-Einstein Condensations from Spin-Orbit Coupling*, *Chin. Phys. Lett.* **28**, 097102 (2011).
  - [21] T.-L. Ho and S. Zhang, *Bose-Einstein Condensates with Spin-Orbit Interaction*, *Phys. Rev. Lett.* **107**, 150403 (2011).

- [22] Y. Zhang, L. Mao, and C. Zhang, *Mean-Field Dynamics of Spin-Orbit Coupled Bose-Einstein Condensates*, *Phys. Rev. Lett.* **108**, 035302 (2012).
- [23] H. Hu, B. Ramachandhran, H. Pu, and X.-J. Liu, *Spin-Orbit Coupled Weakly Interacting Bose-Einstein Condensates in Harmonic Traps*, *Phys. Rev. Lett.* **108**, 010402 (2012).
- [24] T. Ozawa and G. Baym, *Stability of Ultracold Atomic Bose Condensates with Rashba Spin-Orbit Coupling against Quantum and Thermal Fluctuations*, *Phys. Rev. Lett.* **109**, 025301 (2012).
- [25] Y. Li, L. P. Pitaevskii, and S. Stringari, *Quantum Tricriticality and Phase Transitions in Spin-Orbit Coupled Bose-Einstein Condensates*, *Phys. Rev. Lett.* **108**, 225301 (2012).
- [26] Y. Xu, Y. Zhang, and B. Wu, *Bright solitons in spin-orbit-coupled Bose-Einstein condensates*, *Phys. Rev. A* **87**, 013614 (2013).
- [27] Y. Zhang and C. Zhang, *Bose-Einstein condensates in spin-orbit-coupled optical lattices: Flat bands and superfluidity*, *Phys. Rev. A* **87**, 023611 (2013).
- [28] R. Wei and E. J. Mueller, *Magnetic-field dependence of Raman coupling in alkali-metal atoms*, *Phys. Rev. A* **87**, 042514 (2013).
- [29] A. L. Fetter, *Vortex dynamics in spin-orbit-coupled Bose-Einstein condensates*, *Phys. Rev. A* **89**, 023629 (2014).
- [30] M. Gong, S. Tewari, and C. Zhang, *BCS-BEC Crossover and Topological Phase Transition in 3D Spin-Orbit Coupled Degenerate Fermi Gases*, *Phys. Rev. Lett.* **107**, 195303 (2011).
- [31] H. Hu, L. Jiang, X.-J. Liu, and H. Pu, *Probing Anisotropic Superfluidity in Atomic Fermi Gases with Rashba Spin-Orbit Coupling*, *Phys. Rev. Lett.* **107**, 195304 (2011).
- [32] Z.-Q. Yu and H. Zhai, *Spin-Orbit Coupled Fermi Gases across a Feshbach Resonance*, *Phys. Rev. Lett.* **107**, 195305 (2011).
- [33] C. Qu, Z. Zheng, M. Gong, Y. Xu, L. Mao, X. Zou, G. Guo, and C. Zhang, *Topological superfluids with finite-momentum pairing and Majorana fermions*, *Nat. Commun.* **4**, 2710 (2013).
- [34] W. Zhang and W. Yi, *Topological Fulde-Ferrell-Larkin-Ovchinnikov states in spin-orbit-coupled Fermi gases*, *Nat. Commun.* **4**, 2711 (2013).
- [35] C. Chen, *Inhomogeneous Topological Superfluidity in One-Dimensional Spin-Orbit-Coupled Fermi Gases*, *Phys. Rev. Lett.* **111**, 235302 (2013).
- [36] Y. Xu, C. Qu, M. Gong, and C. Zhang, *Competing superfluid orders in spin-orbit-coupled fermionic cold-atom optical lattices*, *Phys. Rev. A* **89**, 013607 (2014).
- [37] F. Lin, C. Zhang, and V. W. Scarola, *Emergent Kinetics and Fractionalized Charge in 1D Spin-Orbit Coupled Flatband Optical Lattices*, *Phys. Rev. Lett.* **112**, 110404 (2014).
- [38] Y. Xu, L. Mao, B. Wu, and C. Zhang, *Dark Solitons with Majorana Fermions in Spin-Orbit-Coupled Fermi Gases*, *Phys. Rev. Lett.* **113**, 130404 (2014).
- [39] L. Jiang, E. Tiesinga, X.-J. Liu, H. Hu, and H. Pu, *Spin-orbit-coupled topological Fulde-Ferrell states of fermions in a harmonic trap*, *Phys. Rev. A* **90**, 053606 (2014).
- [40] Y. Xu and C. Zhang, *Berezinskii-Kosterlitz-Thouless Phase Transition in 2D Spin-Orbit Coupled Fulde-Ferrell Superfluids*, *Phys. Rev. Lett.* **114**, 110401 (2015).
- [41] I. B. Spielman, *Raman processes and effective gauge potentials*, *Phys. Rev. A* **79**, 063613 (2009).
- [42] J. Dalibard, F. Gerbier, G. Juzeliūnas, and P. Öhberg, *Colloquium: Artificial gauge potentials for neutral atoms*, *Rev. Mod. Phys.* **83**, 1523 (2011).
- [43] N. Goldman, G. Juzeliūnas, P. Öhberg, I. B. Spielman, *Light-induced gauge fields for ultracold atoms*, *Rep. Prog. Phys.* **77**, 126401 (2014).
- [44] K. Sun, C. Qu, and C. Zhang, *Spin-orbital angular momentum coupled Bose-Einstein condensates*, *arXiv:1411.1737*.
- [45] Y.-X. Hu, C. Miniatura, and B. Grémaud, *Half-skyrmion and meron pair in spinor condensates*, *arXiv:1410.8634*.
- [46] M. Demarco, and H. Pu, *Angular spin-orbit coupling in cold atoms*, *Phys. Rev. A* **91**, 033630 (2015).
- [47] K.-P. Marzlin, W. Zhang, and E. M. Wright, *Vortex Coupler for Atomic Bose-Einstein Condensates*, *Phys. Rev. Lett.* **79**, 4728 (1997).
- [48] G. Juzeliūnas and P. Öhberg, *Slow Light in Degenerate Fermi Gases*, *Phys. Rev. Lett.* **93**, 033602 (2004).
- [49] N. R. Cooper and Z. Hadzibabic, *Measuring the Superfluid Fraction of an Ultracold Atomic Gas*, *Phys. Rev. Lett.* **104**, 030401 (2010).
- [50] A. Ramanathan, K. C. Wright, S. R. Muniz, M. Zelan, W. T. Hill, C. J. Lobb, K. Helmerson, W. D. Phillips, and G. K. Campbell, *Superflow in a Toroidal Bose-Einstein Condensate: An Atom Circuit with a Tunable Weak Link*, *Phys. Rev. Lett.* **106**, 130401 (2011).
- [51] T.-L. Ho and V. B. Shenoy, *Binary Mixtures of Bose Condensates of Alkali Atoms*, *Phys. Rev. Lett.* **77**, 3276 (1996).
- [52] K. Kasamatsu, M. Tsubota, and M. Ueda, *Vortex Molecules in Coherently Coupled Two-Component Bose-Einstein Condensates*, *Phys. Rev. Lett.* **93**, 250406 (2004).
- [53] M. F. Andersen, C. Ryu, P. Cladé, V. Natarajan, A. Vaziri, K. Helmerson, and W. D. Phillips, *Quantized Rotation of Atoms from Photons with Orbital Angular Momentum*, *Phys. Rev. Lett.* **97**, 170406 (2006).
- [54] C. Ryu, M. F. Andersen, P. Cladé, V. Natarajan, K. Helmerson, and W. D. Phillips, *Observation of Persistent Flow of a Bose-Einstein Condensate in a Toroidal Trap*, *Phys. Rev. Lett.* **99**, 260401 (2007).
- [55] L. S. Leslie, A. Hansen, K. C. Wright, B. M. Deutsch, and N. P. Bigelow, *Creation and Detection of Skyrmions in a Bose-Einstein Condensate*, *Phys. Rev. Lett.* **103**, 250401 (2009).
- [56] N. Lo Gullo, S. McEndoo, T. Busch, and M. Paternostro, *Vortex entanglement in Bose-Einstein condensates coupled to Laguerre-Gauss beams*, *Phys. Rev. A* **81**, 053625 (2010).
- [57] S. Beattie, S. Moulder, R. J. Fletcher, and Z. Hadzibabic, *Persistent Currents in Spinor Condensates*, *Phys. Rev. Lett.* **110**, 025301 (2013).
- [58] S. Moulder, S. Beattie, R. P. Smith, N. Tammuz, and Z. Hadzibabic, *Quantized supercurrent decay in an annular Bose-Einstein condensate*, *Phys. Rev. A* **86**, 013629 (2012).
- [59] P.-P. Huang, C.-A. Chen, H.-J. Wei, C.-Y. Yu, J.-B. Wang, and Y.-J. Lin, *Towards generating synthetic gauge potentials for a Bose-Einstein condensate in a toroidal trap*, 2015 DAMOP (forthcoming) abstract, <http://meetings.aps.org/Meeting/DAMOP15/Session/K1.53>.